




PET imaging of cardiomyocyte apoptosis in a rat myocardial infarction model

Hui Ma¹ · Shaoyu Liu¹ · Ying Xiong¹ · Zhanwen Zhang¹ · Aixia Sun¹ · Shu Su¹ · Hong Liang¹ · Gongjun Yuan¹ · Ganghua Tang¹ 

Published online: 23 June 2018
© Springer Science+Business Media, LLC, part of Springer Nature 2018

Abstract

Cardiomyocyte apoptosis has been observed in several cardiovascular diseases and contributes to the subsequent cardiac remodeling processes and progression to heart failure. Consequently, apoptosis imaging is helpful for noninvasively detecting the disease progression and providing treatment guidance. Here, we tested ¹⁸F-labeled 2-(5-fluoropentyl)-2-methyl-malonic acid (¹⁸F-ML-10) and ¹⁸F-labeled 2-(3-fluoropropyl)-2-methyl-malonic acid (¹⁸F-ML-8) for apoptosis imaging in rat models of myocardial infarction (MI) and compared them with ¹⁸F-fluorodeoxyglucose (¹⁸F-FDG). MI was induced in Sprague-Dawley rats by permanent left coronary artery ligation. Procedural success was confirmed by echocardiography and positron emission tomography (PET) imaging with ¹⁸F-FDG. In vivo PET imaging with ¹⁸F-ML-10 and ¹⁸F-ML-8 was performed in the MI models at different time points after operation. Terminal deoxynucleotidyl transferase dUTP nick-end labeling (TUNEL) assays and immunohistochemical analyses were used to evaluate myocardial apoptosis. In vitro cell binding assays were performed to validate ¹⁸F-ML-8 binding to apoptotic cardiomyocytes. PET imaging demonstrated high ¹⁸F-ML-10 and ¹⁸F-ML-8 uptake where ¹⁸F-FDG uptake was absent. The focal accumulation of the two tracers was high on days 1 and 3 but was not notable on days 5 and 7 after surgery. The infarct-to-lung uptake ratio was 4.29 ± 0.30 for ¹⁸F-ML-10 and 3.51 ± 0.18 for ¹⁸F-ML-8 ($n = 6$, analyzed by averaging the uptake ratios on postoperative days 1 and 3, $P < 0.05$). The TUNEL results showed that myocardial cell apoptosis was closely related to the focal uptake of the apoptotic tracers in the infarct area. In addition, the apoptosis rates calculated from the TUNEL results were better correlated with ¹⁸F-ML-8 uptake than with ¹⁸F-ML-10 uptake. Ex vivo cell binding assays demonstrated that ¹⁸F-ML-8 accumulated in apoptotic cells but not in necrotic or normal cells. PET imaging using ¹⁸F-ML-10 or ¹⁸F-ML-8 allows the noninvasive detection of myocardial apoptosis in the early phase. In addition, ¹⁸F-ML-8 may be better than ¹⁸F-ML-10 for apoptosis imaging. We propose that PET imaging with ¹⁸F-ML-10 or ¹⁸F-ML-8 combined with ¹⁸F-FDG is an alternative for detecting and assessing MI.

Keywords Apoptosis · Myocardial infarction · PET · ¹⁸F-ML-10 · ¹⁸F-ML-8

Introduction

Myocardial infarction (MI) has a high mortality rate and is a major cause of disability worldwide [1]. Apoptosis, an important form of cell death in the early phase of MI, can result in the death of many cardiomyocytes and other types of cells [2]. Thus, apoptosis can cause continuous cardiac cell loss which plays an important role in influencing the final infarct size. Moreover, this damage influences ventricular remodeling and decreases cardiac function [3]. As expected, excessive myocardial cell apoptosis plays a considerable role in the subsequent processes and final outcomes of MI. Additionally, apoptosis can be manipulated and reversed according to the report by Foglio et al. [4]. Thus, the early

✉ Hong Liang
liangh1688@126.com

✉ Ganghua Tang
gtang0224@126.com

¹ Department of Nuclear Medicine and Guangdong Engineering Research Center for the Translational Application of Medical Radiopharmaceuticals, The First Affiliated Hospital, Sun Yat-sen University, Guangzhou 510080, China

detection and inhibition of apoptosis could be a very promising strategy for preventing functional cardiomyocyte loss before it evolves to an irreversible stage. However, apoptosis may have already occurred before the histological changes are conclusive and biological serum tests can detect apoptosis [5, 6]. Therefore, histological examinations and biological serum tests are not suitable for the early detection of apoptosis. However, nuclear imaging, such as single-photon emission computed tomography (SPECT) and positron emission tomography (PET), with apoptotic tracers could identify early apoptosis noninvasively.

During the early phase of apoptosis, changes such as apoptotic scramblase activation, phosphatidylserine (PS) exposure, caspase activation and membrane depolarization occur in cells; these changes can be used as targets for radiopharmaceuticals to bind with [7]. For example, the ^{99m}Tc -labeled Annexin V and the ^{99m}Tc -labeled C2A domain of synaptotagmin I have been reported to detect apoptosis in MI [8, 9]. However, these tracers can bind to exposed PS in both apoptotic and necrotic cells and thus cannot distinguish apoptotic cells from necrotic cells. Recently, Cohen et al. [10] reported on ApoSense family tracers that can discriminate apoptotic and necrotic cells. At present, ApoSense family imaging agents are being used for the in vivo apoptosis detection and imaging. For example, phase I/II clinical trials of ^{18}F -labeled 2-(5-fluoropentyl)-2-methylmalonic acid (^{18}F -ML-10), a low-molecular-weight compound, are already underway [11, 12]. Moreover, Yao et al. [13] also reported that ^{18}F -labeled 2-(3-fluoropentyl)-2-methyl-malonic acid (^{18}F -ML-8), an analog of ^{18}F -ML-10, could be used to assess apoptosis. Compared with ^{18}F -ML-10, ^{18}F -ML-8

has a lower molecular weight and may be more suitable for PET imaging.

To the best of our knowledge, both ^{18}F -ML-10 and ^{18}F -ML-8 have not been applied for PET imaging of apoptosis in MI. Therefore, in this study, PET imaging with ^{18}F -ML-10 and ^{18}F -ML-8 in rat models of MI was performed to detect and assess apoptosis noninvasively.

Materials and methods

Animal study design

This study conformed with the recommendations of the Guide for the Care and Use of Laboratory Animals of the Ministry of Science and Technology of the People's Republic of China. The experimental protocols were approved by the Animal Ethics and Welfare Committee (Permit Number: IACUC-DB-16-1106). Figure 1 depicts the research design, including the number of experimental animals and the time points of different treatments. The animals were divided into 2 groups: the MI group (n=23) and the control group (n=12). On day 0, the MI group was subjected to left anterior descending coronary artery (LAD) ligation, whereas the control animals were sham-operated without LAD ligation. Two rats in the MI group died from severe arrhythmia and heart failure after operation. Rats in the MI group underwent PET imaging with ^{18}F -FDG, ^{18}F -ML-10 or ^{18}F -ML-8 (n=3 for each tracer) on days 1, 3, 5 and 7 after surgery, while the control rats were subjected to the same imaging on only day 1 after surgery (n=3 for each tracer). 3 days after surgery,

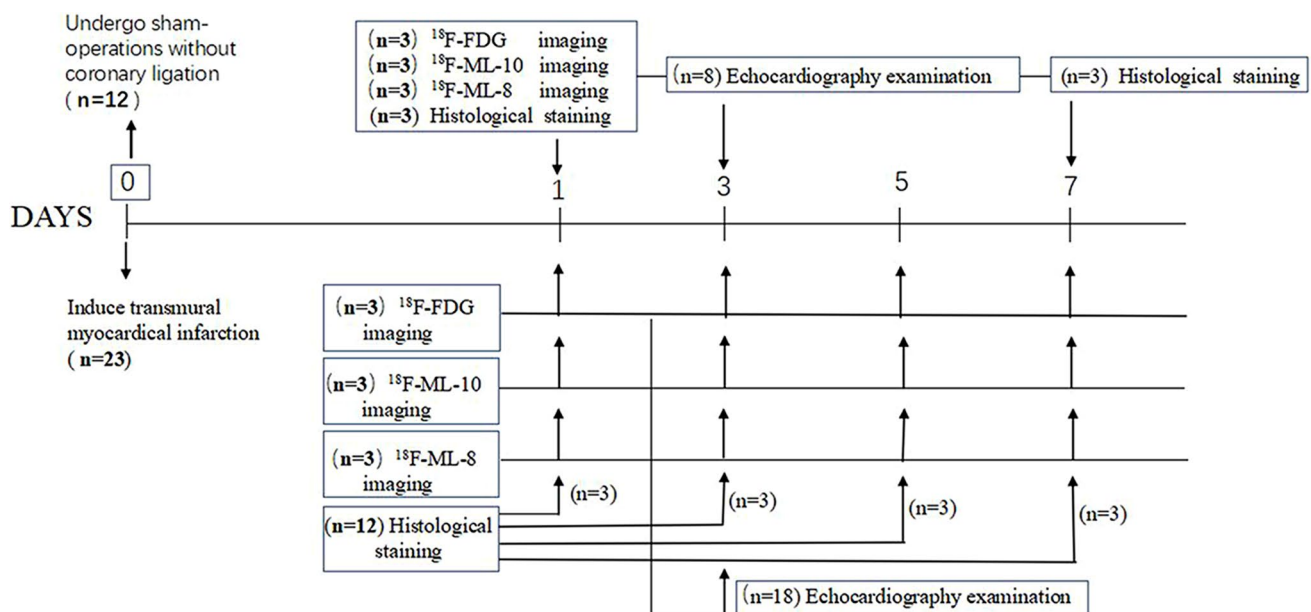


Fig. 1 Outline of the experimental animal design

echocardiography was used to reconfirm the presence of MI and assess cardiac function ($n = 18$ for the MI group; $n = 9$ for the sham group; however, one rat in the sham group died from an anesthesia accident during echocardiography). On days 1, 3, 5, and 7 after surgery, 3 MI animals were sacrificed for *ex vivo* studies, including a series of histological staining: hematoxylin-eosin (HE) staining, Masson trichrome staining, immunohistochemistry with caspase-3 antibody, anti-Bax antibody and anti-Bcl-2 antibody, and terminal deoxynucleotidyl transferase dUTP nick-end labeling (TUNEL) assay. In addition, three sham-operated rats were sacrificed and underwent the same staining procedures on only days 1 and 7 after surgery.

MI induction

Six-week-old male Sprague-Dawley rats were anesthetized with 2% pentobarbital (40 mg/kg) and connected to a small animal ventilator (RWD Life Science, Shenzhen, China). Then, the animals underwent permanent LAD ligation to induce transmural MI as previously described [14–16]. Briefly, LAD occlusion was performed through a left thoracotomy in the fourth intercostal space with a 7–0 suture. The suture was placed 2–3 mm away from the LAD origin and then ligated. Successful occlusion was confirmed by visual myocardial bleaching and ST-segment elevation on an electrocardiogram monitor (Chengdu Techman Software Co.LTD, Chengdu, China). Sham-operated animals, which served as controls, were subjected to a similar surgical procedure. Their pericardium was opened, and a suture was placed under the LAD; however, the suture was not tied around the LAD.

Assessment of cardiac function with echocardiography

Three days after MI, the rats were evaluated by echocardiography using a Vevo 2100 Imaging System with a linear 16–21 MHz transducer (VisualSonics Inc., Toronto, Canada). After anesthesia with 2% isoflurane, the rats were placed on an examination platform, and two-dimensional (2-D) images and M-mode images were obtained at the level of the papillary muscle in the short-axis view. From the 2-D images of the left midventricular level as defined by the American Society of Echocardiography, M-mode images through the papillary muscles were used to measure left ventricular end-diastolic dimension (LVEDD) and left ventricular end-systolic dimension (LVESD) as previously described [17]. In addition, left ventricular fractional shortening (LVFS) and left ventricular ejection fraction (LVEF) were calculated according to the following formulas: $LVFS = (LVEDD - LVESD)/LVEDD \times 100\%$ and $LVEF = (LVEDV - LVESV)/LVEDV \times 100\%$, where LVEDV

indicates the left ventricular end-diastolic volume, and LVESV indicates the left ventricular end-systolic volume. All parameters were obtained from an average of 3 continuous cardiac cycles according to the VisualSonics Vevo 2100 Imaging System Operator Manual.

Small animal PET/computed tomography (CT) imaging

In vivo PET/CT imaging was obtained with the Inveon small animal PET/CT scanner (Siemens). Animals from the two groups were anesthetized with 2% pentobarbital (35 mg/kg) on the 1st day after operation and were injected intravenously with ^{18}F -FDG (37 MBq/kg), ^{18}F -ML-10 or ^{18}F -ML-8 (74 MBq/kg). Afterward, the animals were fixed to remain motionless on a scanning bed with the heart in the center of the field of view. To select an optimal imaging time point, we performed data acquisition in three-dimensional mode at different time points (30, 60, 90 and 120 min) after ^{18}F -ML-10 injection. After that, the same rats of the MI group were scanned on days 3, 5 and 7 postoperatively. All ^{18}F -ML-10 and ^{18}F -ML-8 images were obtained at the optimal time point determined by the aforementioned methods after tracer injection, and ^{18}F -FDG images were obtained 1 h after injection.

After a low-dose CT scan, a 15-min PET scan immediately followed. The CT scan was used for attenuation correction and anatomical localization. Image reconstruction was performed with the two-dimensional ordered-subsets expectation maximum (2D-OSEM). Inveon Research Workplace 4.1 software was used to draw regions of interest (ROIs) of 2 mm in diameter at the same section level of every PET/CT image. In addition, ROIs of the infarct areas were from portions that had negative ^{18}F -FDG uptake, while ROIs of the remote areas were from portions that had positive ^{18}F -FDG uptake. Furthermore, the radioactivity uptake was presented as a percentage of the injected dose per gram of the tissue (%ID/g).

Histological staining

On postoperative days 1, 3, 5 and 7 for the MI group and on postoperative days 1 and 7 for the control group, the rats were anesthetized and sacrificed, and their hearts were excised. Then, 5-mm-thick transverse sections of the hearts 1–2 mm below the ligation were fixed in 4% paraformaldehyde for more than 48 h and then embedded in paraffin. Subsequently, serial 5- μm -thick slices were obtained, and two of these sections were stained separately with HE and Masson trichrome methods. For immunohistochemical staining, primary rabbit monoclonal antibodies against caspase-3 (diluted 1:300, Servicebio, China), Bax (diluted 1:300, Servicebio, China), and Bcl-2 (diluted 1:200, Servicebio,

China) and an HRP-conjugated secondary antibody (Dako, Agilent Technologies, Glostrup, Denmark) were used after conventional processing [18]. Histopathological and immunohistochemical images were captured by a light microscope (Nikon, Tokyo, Japan). Furthermore, five randomly selected fields (magnification, $\times 200$) of the infarct or remote parts of each immunohistochemical section were evaluated by Image-Pro Plus 6.0 software (Media Cybernetics, Rockville, USA) to determine the average integral optical density (IOD) value.

Apoptotic cells were detected by TUNEL assays using an in situ cell death detection kit (Roche, Basel, Germany). All procedures were performed according to the manufacturer's instructions. The images were obtained with an inverted fluorescence microscope (Nikon Eclipse TI-SR, Tokyo, Japan). The cells in ten randomly selected areas were counted (magnification, $\times 400$), and the apoptotic index (AI) was calculated as the number of TUNEL⁺ cell nuclei/total nuclei $\times 100\%$.

Binding assays for ¹⁸F-ML-8 and apoptotic H9C2 cells in vitro

Rat H9C2 cardiomyocytes were kindly provided by the Cell Bank of the Chinese Academy of Sciences in Shanghai. The cells were cultivated in Dulbecco's modified Eagle's medium (DMEM) supplemented with 10% fetal bovine serum, 100 $\mu\text{g/ml}$ streptomycin and 100 IU/ml penicillin at 37 °C in 5% CO₂. When the cells were in the logarithmic growth phase, they were harvested and seeded into six-well plates at the density of 5×10^6 cells/well. After overnight incubation, the cells were divided into five groups and subjected to different treatments. Furthermore, each of the groups was divided into two parallel fractions: one to verify the treatment effect and the other to assess ¹⁸F-ML-8 uptake in apoptotic H9C2 cells.

To induce apoptosis, an anti-Fas antibody (0.2 $\mu\text{g/ml}$) (Abcam, Cambridge, United Kingdom) was added to the H9C2 cells. For the apoptosis inhibition group, H9C2 cells were treated with 50 μM Z-VAD-FMK (Sigma-Aldrich, St. Louis, USA), a pan-caspase inhibitor, 10 min before the addition of anti-Fas. One group without any treatment and another with only inhibitor treatment were included as controls. All cells of the four groups were incubated for 2 h in the culture conditions described above. Finally, the cells were subjected to three freeze–thaw cycles (20 min of freezing at -80 °C, followed by 20 min of thawing at 37 °C) to induce necrosis. After thawing for the last time or after the other treatments listed above, samples were disposed within minutes.

For one cell fraction, the cell culture medium, including floating cells, was collected in different centrifuge tubes. The rest of the cells were then washed twice with

phosphate-buffered saline (PBS) and digested with trypsin without ethylenediamine tetraacetic acid (EDTA). After dissociation, the cells were collected in the corresponding centrifuge tubes mentioned above and pelleted by centrifugation ($1000 \times g$, 5 min). After resuspension in PBS, the cells were centrifuged twice. Next, the cell pellets were resuspended in 100 μl of 1 \times Annexin V buffer. Then, 5 μl of propidium iodide (PI) and 5 μl of AnxV-FITC (apoptosis detection kit, Sigma-Aldrich) were added, and the cells were incubated in the dark for 15 min. Finally, the samples were analyzed by flow cytometry (CytoFLEX, Beckman Coulter, US), and the final data were analyzed by Kaluza software.

For the other cell fraction, the cell culture medium was removed, and 0.22 MBq of ¹⁸F-ML-8 was added to every well of the cells treated as described above. After cultivation for 60 min at 37 °C, the cells were digested with trypsin and collected in respective centrifugation tubes for two cycles of centrifugation and washing with PBS. The cellular uptake activities were measured with a gamma radioimmunoassay counter (SN-6105, Shanghai, China) and presented as the radioactivity per $\sim 10^5$ cells.

Statistical analysis

All values are presented as the mean \pm standard error of the mean (SEM) and were statistically analyzed with GraphPad Prism 6. Unpaired Student's *t* tests were carried out for the analysis of variance between sham-operated and MI animals, and paired Student's *t* tests were used for comparisons between the values obtained on the first and third postoperative days. Values for more than two groups were compared using one-way ANOVA with Geisser-Greenhouse correction, and intergroup comparisons were made using Tukey's multiple comparisons test. Pearson correlation analyses were performed to assess the correlation between the values of two groups, such as the I/L ratios and AI. All differences were considered statistically significant for two-sided *P* values less than 0.05.

Results

Assessment of cardiac function and cardiac morphology

All animals were maintained under the same conditions before the operation. According to the PET/CT images, compared to that in the sham group, there was low or no ¹⁸F-FDG uptake in the anterolateral wall of the left ventricle after MI induction (Fig. 2a). M-mode echocardiography showed that the movement of the anterolateral wall of the MI rats decreased significantly compared to that of the control rats (Fig. 2b). LVEF and LVFS, which were used to assess

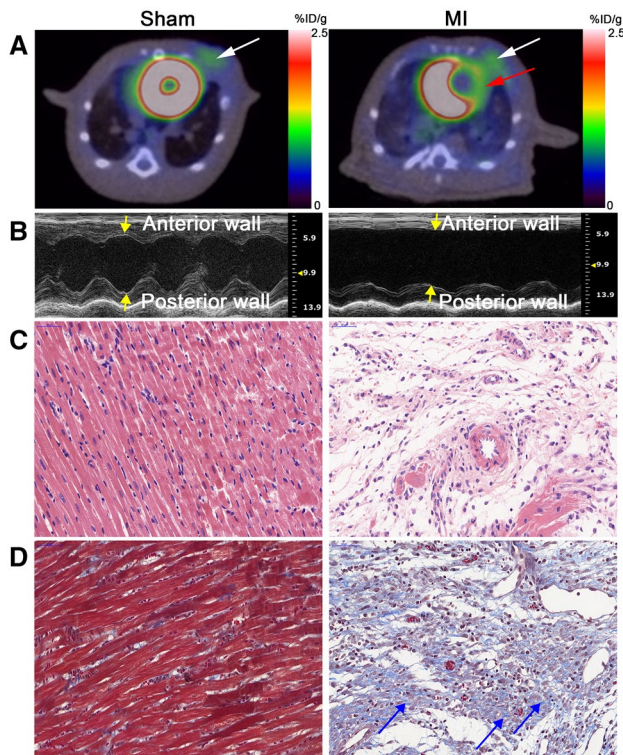


Fig. 2 Representative images of the sham (left) and MI (right) groups. Small animal PET/CT images with ^{18}F -FDG (a) and images captured by M-mode ultrasound (b). There was low uptake (right arrows) and hypokinesia in the anterior walls of MI rats but not in those of sham rats. The white arrows indicate the wound from the operation. HE staining (c, scale bar = 50 μm) and Masson staining (d, scale bar = 50 μm) of the left ventricular myocardium on the 7th day after operations. Cardiomyocytes are stained red, and collagen fibers (blue arrows) are stained blue. After MI, there were many changes in cardiac morphology, such as the disordered and loose arrangement of cardiomyocytes and myocardial fiber hyperplasia. (Color figure online)

cardiac function, were lower in the experimental group than in the control group ($P < 0.0001$; Table 1), but the weight and heart rate differences were not statistically significant between the sham and MI rats ($P > 0.05$; Table 1).

HE and Masson staining on the 7th day after operation indicated morphological discrepancies between the two groups (Fig. 2c, d). Compared to HE and Masson staining in the sham groups, HE staining in the model group revealed a disordered and loose arrangement of the cardiomyocytes (Fig. 2c), while Masson staining in the MI group revealed hyperplasia of the myocardial fibers (Fig. 2d).

In vivo imaging of MI in live rats

As shown in Fig. 3a, the whole heart region was highlighted at 30 min after ^{18}F -ML-10 injection. Over time, an uptake hot-spot became evident in the cardiac area at risk of ischemia. Focused and moderate uptake in the image

Table 1 Comparison of the general characteristics of MI and sham rats on the 3rd day after operation

Parameter	Sham (n = 8)	MI (n = 18)
General characteristics		
Weight (g)	214.6 \pm 2.4	209.9 \pm 1.5
Heart rate (bpm)	381.8 \pm 10.1	365.9 \pm 4.8
Cardiac function parameters		
LVEDD (mm)	6.4 \pm 0.1	8.2 \pm 0.1
LVESD (mm)	3.8 \pm 0.1	6.8 \pm 0.2
LVEF (%)	69.2 \pm 1.7	32.5 \pm 1.4*
LVFS (%)	39.9 \pm 1.3	16.2 \pm 0.78*

On the 3rd day after MI induction, cardiac function was significantly decreased, as assessed by the decrease in LVEF and LVFS, but there were no differences in the weight and heart rate between the sham group and the MI group

* $P < 0.0001$ compared with sham rats

was observed at 120 min after injection; thus, this time point was optimal for apoptosis imaging with ^{18}F -ML-10 and ^{18}F -ML-8. In the sham-operated group (Fig. 3b), tracer uptake in the normal myocardium was gradually washed out, and there was ultimately no uptake hot-spot in the heart.

Importantly, both ^{18}F -ML-10 and ^{18}F -ML-8 uptake were obviously high on the 1st and 3rd days after MI, whereas tracer uptake was not obvious on the 5th and 7th days after the operation. However, Fig. 3c shows that the infarct-to-lung (I/L) uptake ratios of ^{18}F -ML-10 or ^{18}F -ML-8 in the MI rats were not significantly different between the 1st and 3rd days after operation. Then, we calculated the average uptake ratios of the tracers on both days 1 and 3 after operation (subsequently referred to as the first three postoperative days to avoid confusion). Figure 3d shows that the I/L average uptake ratio for the first 3 days was higher for ^{18}F -ML-8 than ^{18}F -ML-10 (4.29 \pm 0.30 vs. 3.51 \pm 0.18; $n = 6$, $P < 0.05$). No significant differences were found in the infarct-to-remote (I/N) uptake ratios of ^{18}F -FDG on different days after operation (Fig. 3e, one-way ANOVA, NS).

On the 1st day after operation, the ^{18}F -FDG PET images could be properly merged with the ^{18}F -ML-10 PET images for the MI rats, showing that the negative uptake of ^{18}F -FDG matched exceedingly well with the hot-spot uptake of ^{18}F -ML-10 in the infarcted myocardium (Fig. 4a). However, ^{18}F -ML-10 images of the sham-operated animals did not show significant tracer uptake (Fig. 4b). Figure 4c shows that there was visible ^{18}F -ML-8 uptake in the left ventricular myocardium and no ^{18}F -FDG uptake in the infarct area of the MI rats. As shown in Fig. 4d, the I/N radioactivity uptake ratios on the first 3 days after operation were 0.25 \pm 0.04, 1.86 \pm 0.05 and 2.50 \pm 0.20 for the MI rats injected with ^{18}F -FDG, ^{18}F -ML-10 and ^{18}F -ML-8 ($n = 6$, $P < 0.0001$, one-way ANOVA), respectively.

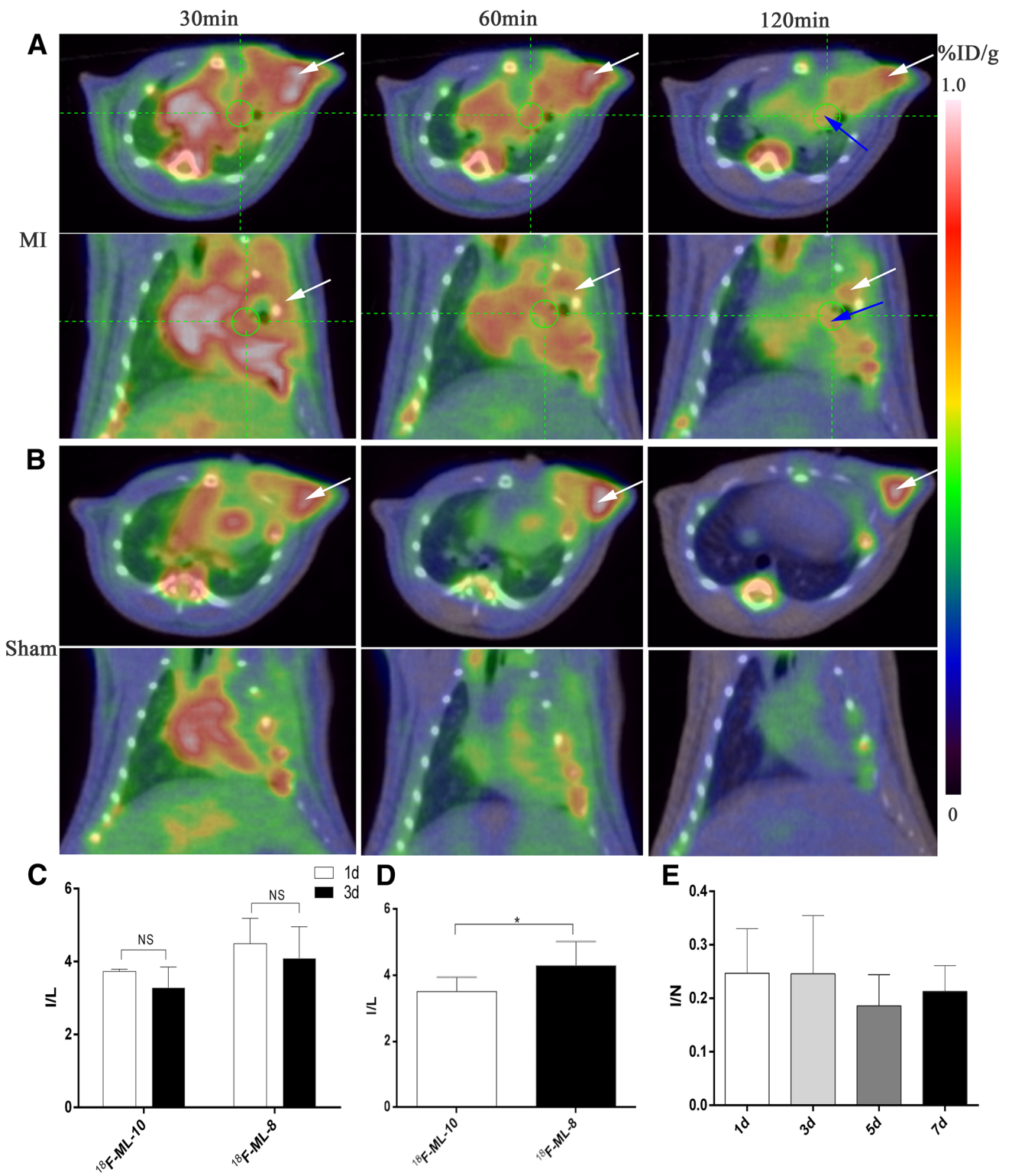
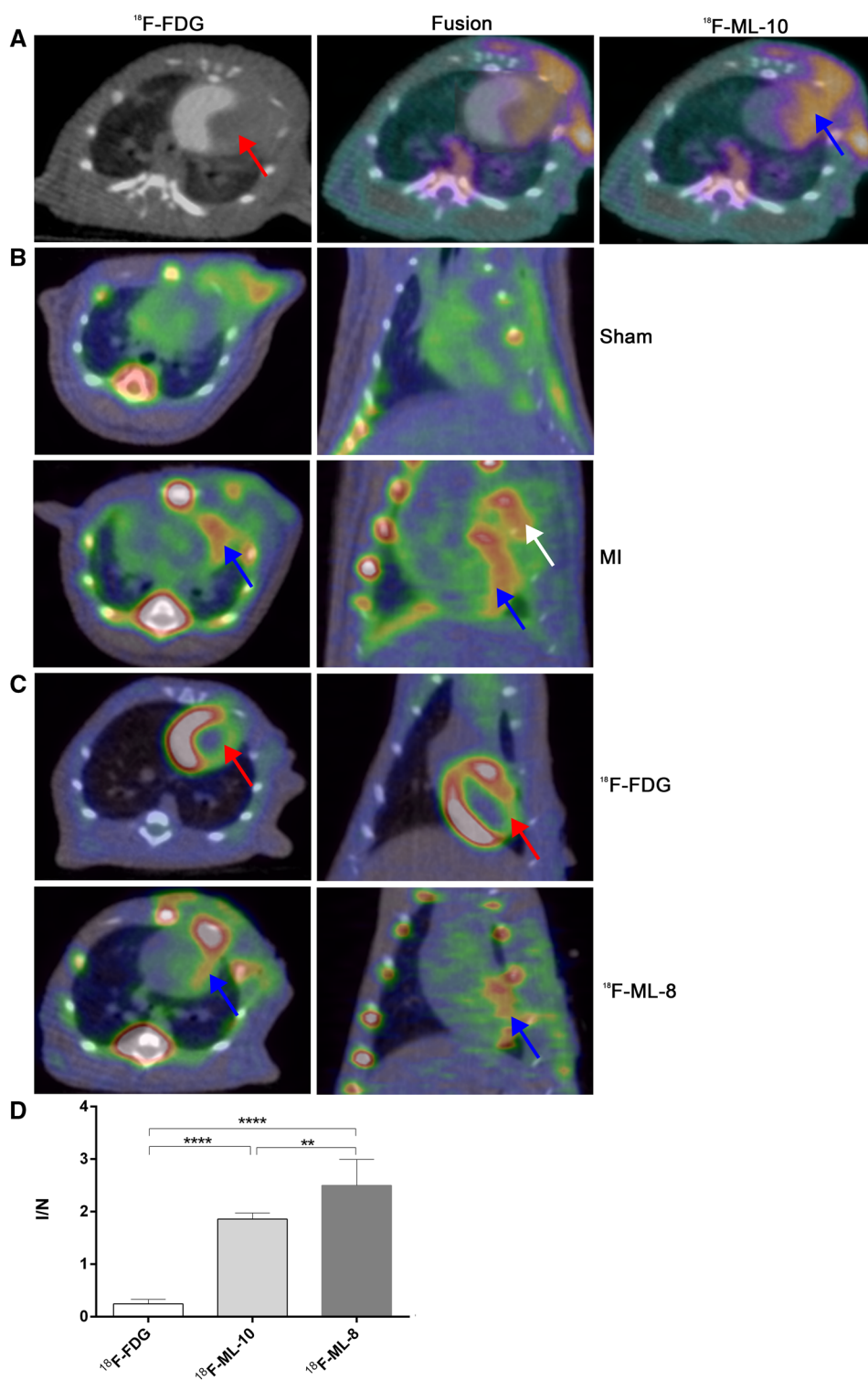


Fig. 3 Representative PET/CT images of MI rats (a) and sham rats (b) at 30, 60 and 120 min after ^{18}F -ML-10 injection. At the top are the transverse images, and at the bottom are the coronal images. c Tracer uptake ratios of the infarct-to-lung (I/L) area for acute MI rats injected with ^{18}F -ML-10 or ^{18}F -ML-8 on the 1st or 3rd days after operation (n=3, NS). d Tracer uptake ratios of the I/L area on the 1st

and 3rd postoperative days were combined to analyze the acute MI rats injected with ^{18}F -ML-10 or ^{18}F -ML-8 (n=6, *P<0.05). e Tracer uptake ratios of the infarct-to-remote (I/N) area for the acute MI rats injected with ^{18}F -FDG on different days after operation (n=3, one-way ANOVA, NS)

Fig. 4 **a** Representative PET/CT images with ^{18}F -FDG (left), ^{18}F -ML-10 (right) and the merged images (middle). **b** Representative transverse (left) and coronal (right) PET/CT images with ^{18}F -ML-10 for sham rats (top) and MI rats (bottom). **c** Representative transverse (left) and coronal (right) PET/CT images with ^{18}F -FDG (top) and ^{18}F -ML-8 (bottom) for MI rats (the red arrows indicate negative uptake; the blue arrows indicate uptake hot-spots; the white arrows indicate the wound uptake). **d** Tracer uptake ratios of the infarct-to-remote (I/N) area in acute MI rats injected with ^{18}F -FDG, ^{18}F -ML-10 or ^{18}F -ML-8 on the first 3 days after operation ($n=6$, $**P<0.01$, $****P<0.0001$). (Color figure online)

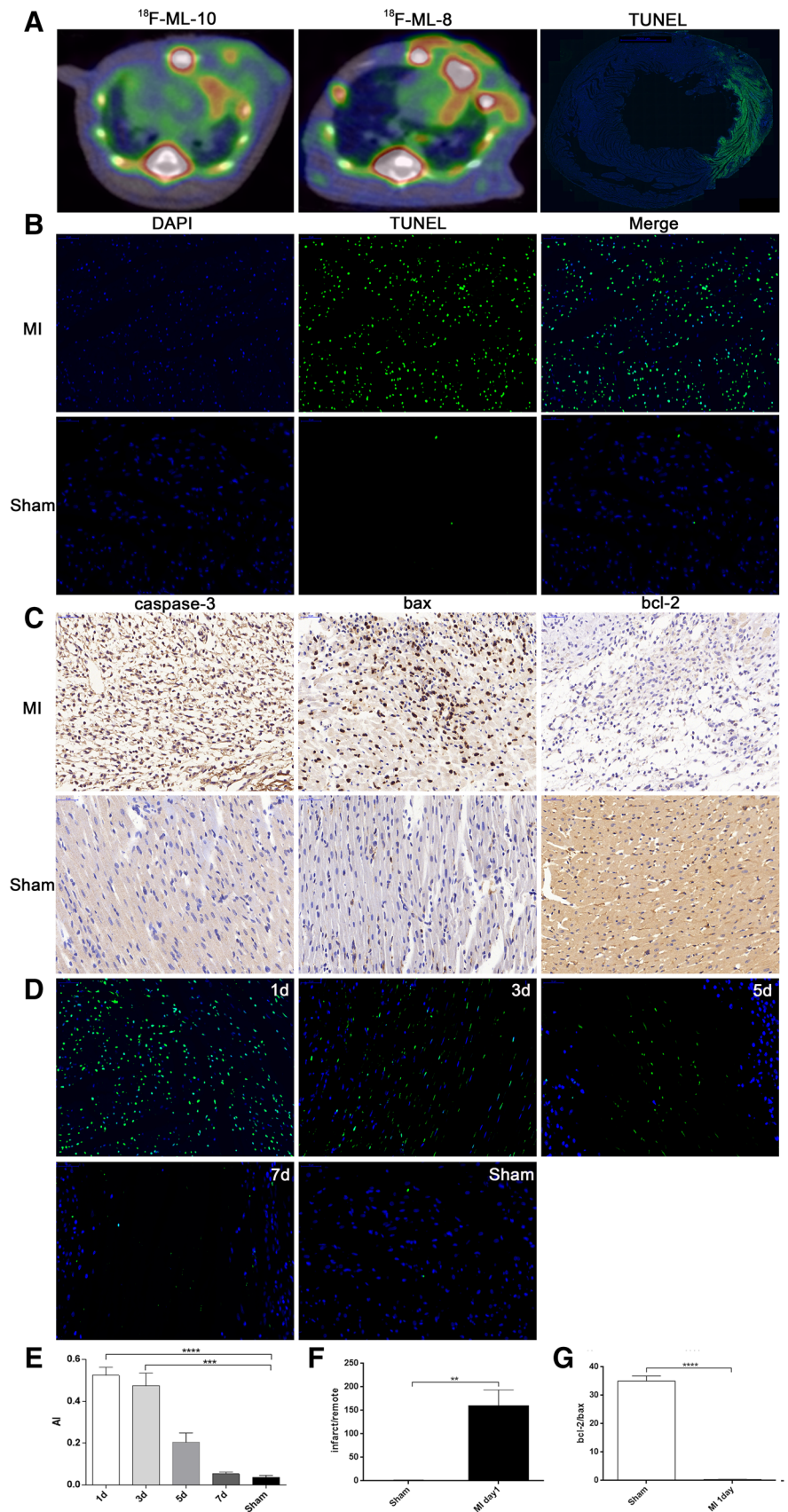


TUNEL and immunohistochemical analyses

The TUNEL-positive areas almost perfectly matched the ^{18}F -ML-10- and ^{18}F -ML-8-positive areas (Fig. 5a). Figure 5b shows the TUNEL results for the MI and sham rats in detail. Moreover, Fig. 5c shows that most of the

TUNEL-positive nuclei were mixed with normal nuclei on the 1st day after operation, while regional TUNEL-positive nuclei prevailed on day 3. Furthermore, the number of apoptotic cells decreased on primarily the 5th and 7th days after operation. In contrast, there were few apoptotic cells in the hearts of sham-operated animals. We calculated

Fig. 5 **a** The TUNEL-positive area (right, scale bar = 2000 μ m) almost perfectly matched the high ^{18}F -ML-10 (left) and ^{18}F -ML-8 (middle) uptake areas in the in vivo PET/CT images. **b** TUNEL staining of the myocardium in MI (top) and sham (bottom) rats (scale bar = 50 μ m). **c** Caspase-3 (left), Bax (middle), and Bcl-2 (right) protein expression (scale bar = 50 μ m). The top figures present the protein expression levels in MI rats, while the bottom figures present the protein expression levels in sham rats. **d** Representative images of TUNEL staining on different days after operation in MI rats and in sham rats (scale bar = 50 μ m). **e** Changes in the AI measured by TUNEL assays on different days after operation. **f** The IOD ratios of the I/N area for caspase-3 protein in the sham group and the MI group on the 1st day after operation. **g** The IOD ratios of Bcl-2/Bax protein in the infarct area for the sham group and the MI group on the 1st day after operation (** $P < 0.01$, *** $P < 0.001$, **** $P < 0.0001$)



the AI from TUNEL images, and the results are shown in Fig. 5e. There were significant differences among the AIs of different groups ($n=3$, $P<0.0001$, one-way ANOVA). Compared to those of the sham group, the AIs of the MI group on the 1st and 3rd days were greatly increased ($n=3$, 0.04 ± 0.01 for the sham group vs. 0.52 ± 0.02 on day 1 and 0.47 ± 0.04 on day 3 after MI induction, each $P<0.0001$). However, there was no obvious difference in the AIs of the MI group between the 1st and 3rd days after operation ($n=3$, 0.52 ± 0.02 on day 1 vs. 0.47 ± 0.04 on day 3, NS). In addition, the same result was observed between the 7th day and the sham group ($n=3$, 0.05 ± 0.01 on day 7 vs. 0.04 ± 0.01 for the sham group, NS).

Other types of immunohistochemical staining were also compared on the first day after operation. Caspase-3 and Bax protein expression levels were higher in the MI rats than in the sham rats, while Bcl-2 protein expression levels were lower in the MI rats than in the sham rats (Fig. 5d). For caspase-3 staining, the IOD ratio of the I/N area was 159.95 ± 19.34 for the MI group on the 1st day and was significantly higher than that of the sham rats (1.68 ± 0.16 , $P<0.01$, Fig. 5f). In addition, the IOD ratio of Bcl-2 to Bax in the infarct area was considerably lower than that of the sham rats (0.38 ± 0.07 vs. 35.00 ± 1.04 , $P<0.0001$) (Fig. 5g).

Correlations between AI and ^{18}F -FDG, ^{18}F -ML-10 and ^{18}F -ML-8 uptake

We investigated whether there were correlations between the degree of apoptosis and tracer uptake calculated from the ^{18}F -FDG, ^{18}F -ML-10 or ^{18}F -ML-8 PET images, particularly on the 1st and 3rd postoperative days. We calculated the I/L uptake ratios on the first 3 days according to the ^{18}F -FDG, ^{18}F -ML-10 and ^{18}F -ML-8 images. Figure 6a shows that there was no correlation between the AI and the I/L uptake ratio of ^{18}F -FDG ($P>0.5$). Conversely, a positive correlation was found between the AI and apoptotic tracer

uptake ($R^2=0.73$ for ^{18}F -ML-10 and 0.74 for ^{18}F -ML-8, both $P<0.05$, Fig. 6b, c).

In vitro binding assays of ^{18}F -ML-8 and apoptotic cells

To verify apoptotic tracer accumulation in apoptotic cells, we performed in vitro binding assays using ^{18}F -ML-8 and apoptotic H9C2 cells; ^{18}F -ML-10 binding with apoptotic cells has already been demonstrated by Cohen et al. [10]. Flow cytometry analysis of the cells treated as described above confirmed that apoptosis and necrosis were induced successfully (Fig. 7a). According to flow-cytometric density plots, the sum of Q2 and Q3, which represents apoptotic cells in the anti-Fas-treated group (Fig. 7a, in the middle, approximately 44%), was the highest of all the different treatment groups. The sum of Q4, which indicates necrotic cells, was particularly high in the freeze-thaw treatment group (Fig. 7a, on the right side). In addition, the results of the control group are shown on the left side of Fig. 7a. According to the binding assays, the radioactivity value in anti-Fas-treated cells (0.32 ± 0.01 CPM/ 10^5 cells) was twice as high as that in control cells (0.16 ± 0.01 CPM/ 10^5 cells) (Fig. 7b). In contrast, after the addition of the caspase inhibitor Z-VAD-FMK to inhibit apoptosis, there was no difference in the radioactivity uptake value of ^{18}F -ML-8 between the control and inhibited groups (Fig. 7b). Similarly, there was no apparent ^{18}F -ML-8 uptake by the cells in the necrotic group (Fig. 7b). These results indicated that ^{18}F -ML-8 was taken up by the apoptotic cells but not by the necrotic or normal cells.

Discussion

^{18}F -FDG images have long been considered as the gold standard for assessing myocardial metabolic viability [19]. However, PET imaging with ^{18}F -FDG is not suitable for

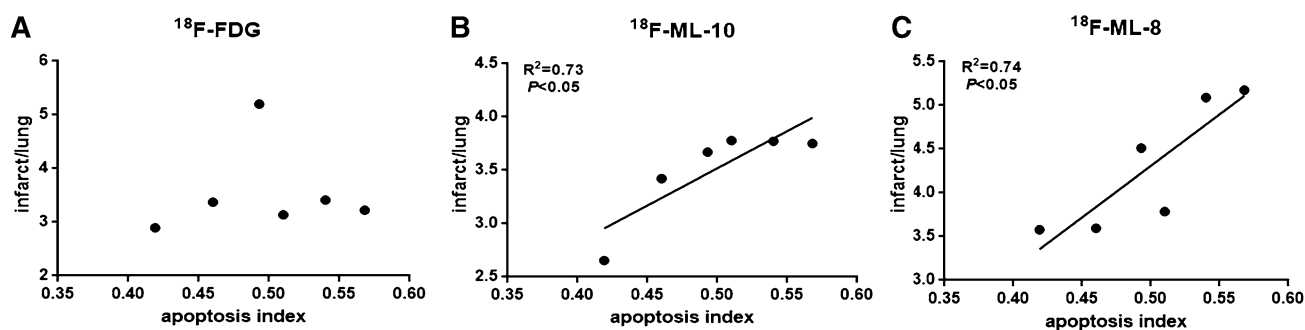


Fig. 6 Correlation between the AI and ^{18}F -FDG uptake (a), ^{18}F -ML-10 uptake (b) and ^{18}F -ML-8 uptake (c). The uptake values are presented as the tracer uptake ratios of the infarct area to the lung

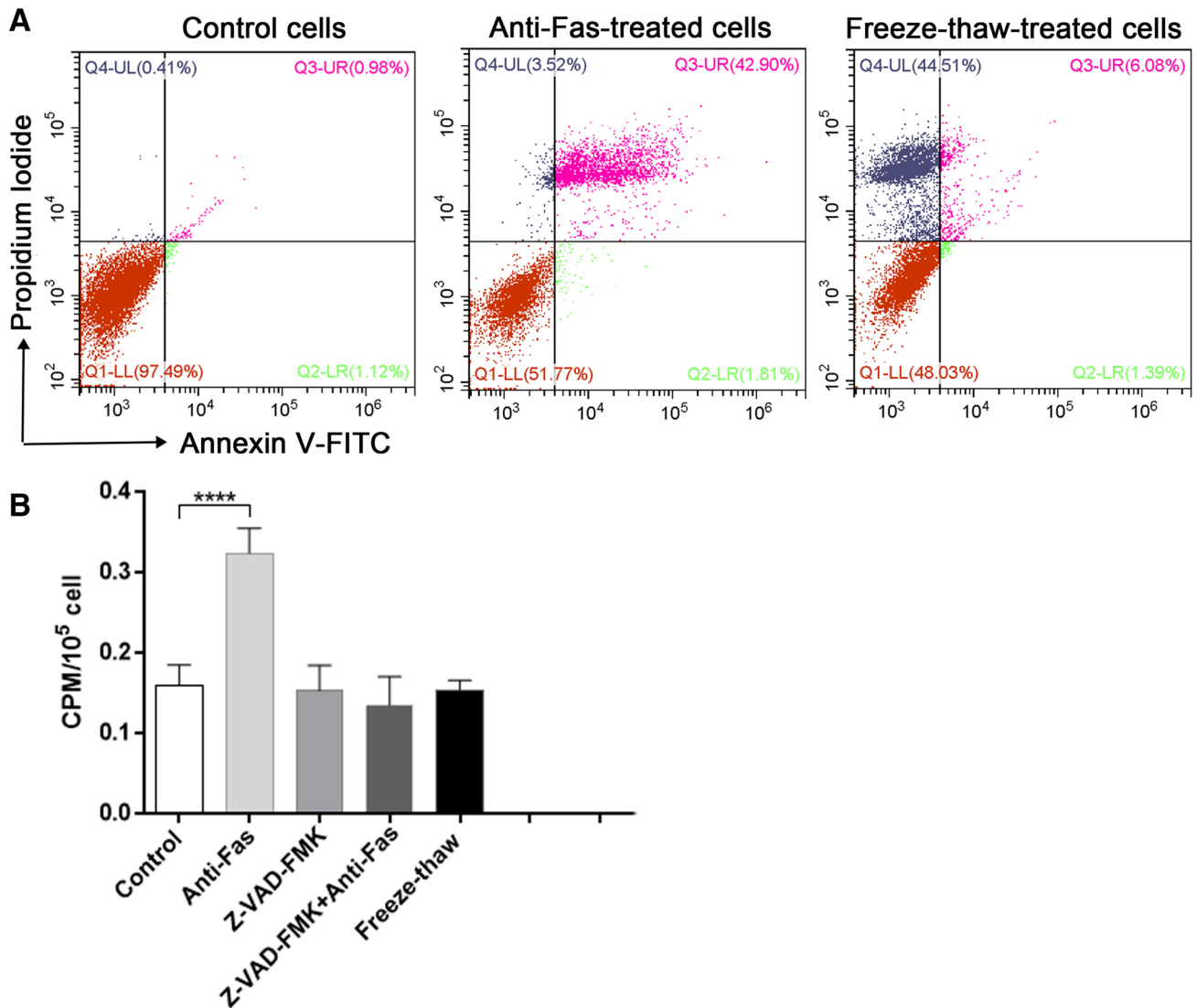


Fig. 7 Flow cytometry and cell binding assay results. **a** Results for the control group (left), the anti-Fas-treated group (middle), and the freeze-thaw-treated group (right). **b** ^{18}F -ML-8 uptake by cells in the various treatment groups. **** $P < 0.0001$

detecting apoptosis because there is negative uptake in the infarct area and no correlation between ^{18}F -FDG uptake and apoptosis according to our study. Therefore, we used tracers from the ApoSense family (^{18}F -ML-10 and ^{18}F -ML-8) to perform PET imaging of apoptosis in a rat MI model for the first time. Our study proved that the positive uptake of ^{18}F -ML-10 and ^{18}F -ML-8 as apoptotic tracers matched the negative uptake of ^{18}F -FDG in the infarction area. Moreover, there was a relationship between myocardial apoptosis and tracer uptake in the infarct area, which could provide a new method for characterizing the progression and prognosis of MI in its early stage. As a result, PET imaging with ^{18}F -ML-10 or ^{18}F -ML-8 combined with ^{18}F -FDG could be an alternative for detecting and assessing MI.

Members of the ApoSense family have been used as apoptotic tracers because they bind to the apoptotic membrane imprint in the early phase of apoptosis [20]. In addition, ^{18}F -ML-10 and ^{18}F -ML-8, as small-molecule probe compounds, have been reported to selectively target and consequently accumulate in apoptotic cells [10, 13]. In our study, we also used in vitro flow cytometry and cell binding assays to show that ^{18}F -ML-8 bound to apoptotic cells rather than necrotic cells. In vivo, there was first a high blood concentration of the tracer after ^{18}F -ML-10 injection. Then, the tracer infiltrated the apoptotic area and bound to the apoptotic cells. Due to gradual washout, there was finally specific uptake in only the apoptotic area. In addition, as an analog of ^{18}F -ML-10, ^{18}F -ML-8 should have the same dynamic uptake process

as ^{18}F -ML-10. In conclusion, ^{18}F -ML-10 and ^{18}F -ML-8 can differentiate apoptosis from necrosis.

Several studies have reported that other radiotracers could also be used for the molecular imaging of apoptosis in MI models. Zhao et al. [9], Niu et al. [21] and Sun et al. [22] have respectively reported on $^{99\text{m}}\text{Tc}$ -C2A-GST, $^{99\text{m}}\text{Tc}$ -annexin V and ^{18}F -FP-DPAZn2; however, these tracers could not differentiate apoptosis from necrosis. Han et al. [23] recently reported that ^{18}F -NaF enabled the noninvasive imaging of MI. However, they did not further elaborate on the relation between ^{18}F -NaF uptake and apoptotic cells or necrotic cells. Unlike the results from previous studies, ^{18}F -ML-10 and ^{18}F -ML-8 could not only distinguish the two forms of cell death but also define the presence, position and extent of apoptosis in our study. Additionally, ^{18}F -ML-8 could be a better tracer for imaging MI than ^{18}F -ML-10. Importantly, ^{18}F -ML-8 has a similar structure but a smaller molecular weight than ^{18}F -ML-10, which could enable a higher target-to-background ratio than ^{18}F -ML-10 imaging. Moreover, the apoptosis rate and the uptake ratio of I/L were better correlated for ^{18}F -ML-8 imaging than for ^{18}F -ML-10 imaging in this study.

In our study, uptake hot-spots for ^{18}F -ML-10 and ^{18}F -ML-8 imaging were found on days 1 and 3 postoperation; in vitro TUNEL staining in vitro confirmed that there were many apoptotic cells at these time points. In contrast, there was no evident uptake of the tracers in the same MI area on the 5th and 7th postoperative days when few apoptotic cells were found by TUNEL staining in vitro. Therefore, we think that PET imaging using these apoptotic tracers can provide visual detection only when there are many apoptotic cells in the early infarcted myocardium, and that the optimal time window is the first 3 days after MI onset. This proposal is consistent with the observation that apoptotic myocytes were present at 4 h following permanent coronary occlusion, reached the maximum amount at 18 h, remained constant until 48 h, and decreased at 72 h according to the report by Bialik et al. [24]. Moreover, the association between ^{18}F -ML-10 and ^{18}F -ML-8 uptake and the extent of myocardial apoptosis, which was confirmed by the correlation analysis on postoperative days 1 and 3, could be the basis for quantifying early myocardial injury. Therefore, using apoptotic tracers for the early clinical noninvasive identification and localization of myocardial apoptosis is promising; this information could also be helpful in clinical decision-making. Nevertheless, further studies should be performed to verify imaging with these tracers at earlier time points, such as at approximately 4 h postoperatively.

There are also some limitations to this study. First, the infarct size was not quantified in this study. Consequently, the evidence provided for the tracers may be insufficient to evaluate treatment responses in our current work. Further studies, such as correlation analyses for cardiac function and

tracer uptake after certain treatments, should be performed. Second, the ^{18}F -ML-8 uptake hot-spot seems to be extracardiac, with a very weak signal in the infarct area (shown in Fig. 4c). This finding may be due to minor amounts of ^{18}F -anion in the final product, a low specific concentration or specific activity, and operative wound and defense reactions, all of which may play an important role in causing the high levels of non-specific ^{18}F -ML-8 uptake. Additionally, the small number of apoptotic cardiomyocytes may have led to weak tracer uptake in the infarct area. Finally, it may also take a long time to obtain high-quality images after tracer injection. As a result, more studies of apoptotic imaging with ^{18}F -ML-10 and ^{18}F -ML-8 are still needed.

Conclusion

In this study, we successfully imaged apoptosis in MI with ^{18}F -ML-10 and ^{18}F -ML-8, and these tracers produced better results than ^{18}F -FDG. ^{18}F -ML-8 showed a higher target-to-background ratio than ^{18}F -ML-10 in the MI model. The apoptosis analysis demonstrated that ^{18}F -ML-8 uptake was better correlated with the apoptosis rate than ^{18}F -ML-10 uptake or ^{18}F -FDG uptake. In conclusion, PET images with ^{18}F -ML-10 and ^{18}F -ML-8 can provide a novel approach for early noninvasive apoptosis detection in MI; these data could be used for quantifying early myocardial injury in a short time window. Importantly, ^{18}F -ML-8 appears to be a better tracer than ^{18}F -ML-10 for apoptotic imaging.

Acknowledgements This work was supported in part by the Science and Technology Foundation of Guangdong Province (Nos. 2014A020210008 and 2016B090920087), the Science and Technology Planning Project Foundation of Guangzhou (Nos. 201604020169 and 201510010145), the National Natural Science Foundation of China (Nos. 81571704, 81671719 and 81770505), the Natural Science Foundation of Guangdong Province (No. 2015A030313067), and the Research Project of Shanghai Municipal Health and Family Planning Commission (No. 201740060).

Compliance with ethical standards

Conflict of interest The authors declare that they have no conflict of interest.

References

1. Thygesen K, Alpert JS, Jaffe AS et al (2012) Third universal definition of myocardial infarction. *Eur Heart J* 33:2551–2567
2. Kajstura J, Cheng W, Reiss K et al (1996) Apoptotic and necrotic myocyte cell deaths are independent contributing variables of infarct size in rats. *Lab Invest* 74:86–107
3. Zhang Q, Yu N, Yu BT (2018) MicroRNA-298 regulates apoptosis of cardiomyocytes after myocardial infarction. *Eur Rev Med Pharmacol Sci* 22(2):532–539

4. Foglio E, Puddighinu G, Germani A et al (2017) HMGB1 inhibits apoptosis following MI and induces autophagy via mTORC1 inhibition. *J Cell Physiol* 232(5):1135–1143
5. Lotats A, Carrió I (2003) Non-invasive in vivo imaging of myocardial apoptosis and necrosis. *Eur J Nucl Med Mol Imaging* 30(4):615–630
6. Rodríguez M, Lucchesi BR, Schaper J (2002) Apoptosis in myocardial infarction. *Ann Med* 34(6):470–479
7. Reshef A, Shirvan A, Wall A et al (2010) Small-molecule biomarkers for clinical PET imaging of apoptosis. *J Nucl Med* 51:837–840
8. Sarda-Mantel L, Michel JB, Rouzet F et al (2006) ^{99m}Tc -annexin V and ^{111}In -antimyosin antibody uptake in experimental myocardial infarction in rats. *Eur J Nucl Med Mol Imaging* 33:239–245
9. Zhao M, Zhu X, Ji S et al (2006) ^{99m}Tc -labeled C2A domain of synaptotagmin I as a target-specific molecular probe for non-invasive imaging of acute myocardial infarction. *J Nucl Med* 47:1367–1374
10. Cohen A, Shirvan A, Levin G et al (2009) From the Gla domain to a novel small-molecule detector of apoptosis. *Cell Res* 19:625–637
11. Allen AM, Ben-Ami M, Reshef A et al (2012) Assessment of response of brain metastases to radiotherapy by PET imaging of apoptosis with ^{18}F -ML-10. *Eur J Nucl Med Mol Imaging* 39:1400–1408
12. Oborski MJ, Laymon CM, Lieberman FS et al (2014) First use of ^{18}F -labeled ML-10 PET to assess apoptosis change in a newly diagnosed glioblastoma multiforme patient before and early after therapy. *Brain Behav* 4:312–315
13. Yao S, Hu K, Tang G et al (2015) Molecular PET Imaging of cyclophosphamide induced apoptosis with ^{18}F -ML-8. *Biomed Res Int* 2015:1–10
14. Patten RD, Aronovitz MJ, Deras-Mejia L et al (1998) Ventricular remodeling in a mouse model of myocardial infarction. *Am J Physiol* 274:H1812–H1820
15. Gao XM, Dart AM, Dewar E et al (2000) Serial echocardiographic assessment of left ventricular dimensions and function after myocardial infarction in mice. *Cardiovasc Res* 45:330–338
16. Ahn D, Cheng L, Moon C et al (2004) Induction of myocardial infarcts of a predictable size and location by branch pattern probability-assisted coronary ligation in C57BL/6 mice. *Am J Physiol Heart Circ Physiol* 286:H1201–H1207
17. Wu JC, Chen IY, Wang Y et al (2004) Molecular imaging of the kinetics of vascular endothelial growth factor gene expression in ischemic myocardium. *Circulation* 110:685–691
18. Aboutaleb N, Shamsaei N, Khaksari M et al (2015) Pre-ischemic exercise reduces apoptosis in hippocampal CA3 cells after cerebral ischemia by modulation of the Bax/Bcl-2 proteins ratio and prevention of caspase-3 activation. *J Physiol Sci* 65:435–443
19. Jr SJ, Rodrigues FF, Izaki M et al (2014) Low-carbohydrate diet versus euglycemic hyperinsulinemic clamp for the assessment of myocardial viability with ^{18}F -fluorodeoxyglucose-PET: a pilot study. *Int J Cardiovasc Imaging* 30(2):415–423
20. Reshef A, Shirvan A, Akselrod-Ballin A et al (2010) Small-molecule biomarkers for clinical PET imaging of apoptosis. *J Nucl Med* 51:837–840
21. Niu G, Hen X (2010) Apoptosis imaging: beyond annexin V. *J Nucl Med* 51:1659–1662
22. Sun T, Tang G, Hua T et al (2015) Positron emission tomography imaging of cardiomyocyte apoptosis with a novel molecule probe [^{18}F]FP-DPAZn2. *Oncotarget* 6:30579–30591
23. Han JH, Lim SY, Lee MS et al (2015) Sodium [^{18}F]fluoride PET/CT in myocardial infarction. *Mol Imaging Biol* 17:214–221
24. Bialik S, Geenen DL, Sasson IE et al (1997) Myocyte apoptosis during acute myocardial infarction in the mouse localizes to hypoxic regions but occurs independently of p53. *J Clin Invest* 100:1363–1372